A computational framework for meso and macroscale analysis of structural masonry

K. Koocheki [a], S. Pietruszczak [a,*], E. Haghighat [b]

[a] *McMaster University, Hamilton, ON, Canada*
[b] *University of British Columbia, Vancouver, BC, Canada*

ABSTRACT

In this study a computational framework is outlined for modeling the mechanical response of structural masonry at both meso and macroscale. The mesoscale approach accounts for the presence of distinct constituents (i.e., bricks and mortar joints) and their geometric arrangement. A constitutive law with embedded discontinuity, combined with the level-set approach, is used to model the onset and discrete propagation of localized damage in these constituents. The approach is verified against a range of experimental data published in the literature. It is shown that the proposed framework can adequately predict the load-deformation response, as well as the fracture pattern under combined loading conditions. The macroscale approach incorporates the notion of anisotropy parameter whose value depends on the orientation of the principal stress axes in relation to the axes of material symmetry. The material parameters/function appearing in this approach are identified from the 'virtual data' generated by a mesoscale analysis of masonry panels subjected to biaxial tension–compression at different orientations of the bed joint. Thus, the mesoscale considerations serve as a bridge for upscaling to the macrolevel.

1. Introduction

Numerical analysis of masonry structures can be conducted at either meso or macroscale. The former approach is suitable for smaller scale structures (e.g., shear walls, reduced scale models, etc.). For large structures (buildings, arch bridges, etc.), however, examining individual components (i.e., units/joints) and their interaction would be computationally very costly. Therefore, a more reasonable approach is that in which the masonry is considered as a continuum with a microstructure.

In engineering practice, the design and retrofit of masonry structures follows a set of guidelines provided by different building codes. The methodologies employed in these codes, i.e. limit state design and/or empirical methods, are quite simplistic. They do not address the basic issues that govern the mechanical response of masonry at the macroscale, such as the anisotropy of strength and deformation properties, discrete propagation of damage, environmental degradation, etc. Thus, although the general guidelines are useful, they are primarily qualitative and cannot be perceived as a reliable mechanical assessment, particularly when dealing with structures of a strategic importance that often have a complex geometry.

A better representation of the behaviour of structural masonry may be obtained by conducting the finite element (FEM) analysis. In recent years this has become a standard in the engineering design process. For the *mesoscale* simulations, the constituents themselves (i.e. units and mortar joints) may be considered as isotropic (Minga et al., 2018). In this case, the primary difficulty is to deal with the notion of localized deformation. The latter involves the presence of discontinuities in the displacement field or its gradient, referred to as *strong* or *weak* discontinuities (Simo et al., 1993), and is associated with the strain-softening response. In this case, the use of classical continuum approaches, which do not incorporate any measure of internal scale, results in a spurious mesh-dependency of the solution. In order to remedy the problem, the constitutive equations have been enhanced to incorporate non-local theories (Bažant & Jirásek, 2002; Jirásek, 2004) or visco-plastic regularization (Needleman, 1988; Niazi et al., 2012). Both these approaches, however, have limitations that stem from ambiguity in specifying the characteristic length and/or the viscosity parameter, which are not uniquely defined. Moreover, such continuum enhancements do not explicitly incorporate the rate form of traction– displacement discontinuity relation for the fracture zone, which is intrinsic in describing the softening phenomenon.

---

* Corresponding author.
  E-mail address: pietrusz@mcmaster.ca (S. Pietruszczak).

An alternative way to deal with localized deformation is to invoke the embedded discontinuity approach (cf. Wells & Sluys, 2000, 2001; Jirasek and Zimmermann, 2001; Alfaiate et al., 2003; Benkemoun et al., 2010). In this approach, the discontinuities are embedded directly within a *finite element*. Both weak and strong discontinuities can be dealt with by addition of discontinuous functions to either strain or displacement fields of standard finite elements. In case of strong discontinuities, additional global degrees of freedom, i.e. nodal displacements associated with enhanced modes, are introduced and additional shape functions are added. There are different versions of the embedded discontinuity formulation including discrete approaches in which the crack path and the displacement jumps are continuous across element boundaries. The literature on this topic is very extensive and a comprehensive survey, which includes a comparison between various approaches, is provided in Jirásek (2000). Another enrichment technique, which has been developed in the context of partition of unity method, is the Extended Finite Element Method (XFEM) (Belytschko et al., 2001; Belytschko & Black, 1999; Moës & Belytschko, 2002). Again, a comparative study of this approach in relation to other FE techniques for capturing strong discontinuities is provided by Oliver et al. (2006).

Both the above-mentioned approaches are rigorous and have been applied to a broad spectrum of engineering problems. Their main limitation, particularly in case of XFEM, is a high computational cost that stems primarily from incorporation of additional degrees of freedom that account for the presence of discontinuities. The approach employed in this work is conceptually different in the sense that the velocity discontinuity is explicitly embedded in the *constitutive law*. The latter incorporates a length scale parameter, which is defined in an explicit manner. The approach was originally proposed in the early 1980′s (Pietruszczak and Mróz, 1981) and was later modified to redefine the internal length parameter (cf. Pietruszczak, 1999). Its implementation in the FEM platform is straightforward, as no enriched degrees of freedom are required. An enhanced version, which incorporates a discrete crack tracing scheme, is provided in Haghighat & Pietruszczak (2015, 2016). The last references also give a direct comparison of the numerical performance of this approach in relation to XFEM methodology.

The *macroscale* analysis requires the assessment of equivalent mechanical properties for a given type of masonry layout. This can be accomplished by application of the mathematical theories of homogenization. The latter have been applied in the context of both periodic (Sacco, 2009; Anthoine, 1997; De Buhan & De Felice, 1997; Pande et al., 1989) as well as non-periodic media (Cluni & Gusella, 2004) and a comprehensive review of different strategies is provided in Lourénço et al. (2007). The main difficulty in this approach is the assessment of properties in inelastic range, which requires a numerical homogenization. In this case, the simulations are carried out using a representative elementary volume (REV) from which the equivalent (i.e., volume averaged) properties are acquired (e.g., Van der Sluis et al., 2000). The computational homogenization techniques have also been extensively used in the context of multiscale modeling of heterogeneous materials with complex microstructures. The literature on this topic is very extensive and a concise review is provided, for example, in Geers et al. (2010). The approach comprises a multi-level finite element analysis, referred to as FE^2 scheme (cf. Smit et al., 1998; Feyel, 2003; Nguyen et al., 2011), which employs meshing at macro-level (entire structure) and micro-level (REVs). An application of this methodology to masonry, involving simulation of some material tests as well as a shear wall test, is provided by Massart et al. (2007). The approach is rigorous, but computationally very expensive and its application in the context of large-scale masonry structures is currently not feasible.

In general, the key issues in modeling the mechanical response of masonry at the macroscale involve a proper description of inherent anisotropy and, once again, the localized nature of damage. The anisotropy manifests itself in the directional dependence of strength and deformation properties. This has been evidenced by testing scaled masonry panels under biaxial load at different orientations of the bed joints (c.f. Drysdale & Khattab, 1995; Page, 1981; Page, 1983). The results of these tests provided a valuable information that has been employed to specify the conditions at failure. The existing formulations defining the phenomenologically based failure criteria usually incorporate linear and quadratic terms in stress components referred to as principal material axes (e.g. Tsai & Wu, 1971). Examples of application of this class of criteria to structural masonry include the work of Lourénço et al. (1997) and Berto et al. (2002). A more rigorous approach is associated with incorporating the notion of a fabric tensor and establishing its correlation with the strength properties (Boehler & Sawczuk, 1977; Cowin, 1986). The disadvantage of the latter approach, however, is the fact that the general framework incorporates numerous material functions whose identification requires an elaborated experimental program which cannot be carried out for any practical engineering problem. A simplified and a more pragmatic methodology was introduced by Pietruszczak & Mroz (2001) whereby the classical isotropic criteria have been enhanced by incorporating the concept of a spatial distribution of strength parameters. Two different approaches have been developed, viz. a critical plane and a microstructure tensor approach. In the former, the failure criterion is expressed in terms of traction components, while the orientation of the localization plane is defined as a constrained optimization problem. In the approach incorporating the microstructure tensor, a scalar anisotropy parameter is introduced whose value is a function of relative orientation of the principal stress triad with respect to the eigenvectors of the microstructure tensor. The latter methodology has recently been applied by Pietruszczak and Mohammadi (2020) to define the macroscopic failure criterion using the experimental data reported by Page (1981, 1983).

This paper is a continuation of the work reported by Pietruszczak and Mohammadi (2020). Its primary focus is the development of a reliable computational scheme for the mesoscale analysis of structural masonry. The approach incorporates a novel technique for dealing with the bed and head joints, whose presence is accounted for by employing a constitutive law with embedded discontinuity (Haghighat & Pietruszczak, 2015). This allows the use of a simple structured mesh which significantly reduces the computational cost of analysis. The procedure also accounts for the onset of new macrocracks forming within the masonry units and the discrete tracing of their propagation by means of the level set technique. The purpose of this mesoscale approach is two-fold. First, such an approach can be used for an independent analysis of smaller scale masonry structures. At the same time, it can serve the purpose of generating a 'virtual data' for masonry panels tested at different orientations relative to the direction of loading. The latter information can then be employed in the context of specification of material functions required for the analysis of large masonry structures. Thus, the mesoscale considerations serve as a bridge for upscaling to the macroscale.

In the next section the mesoscale formulation and its numerical implementation are discussed. Subsequently, the framework is verified against some benchmark problems involving simulation of experimental tests on brick–mortar bond and masonry wallets. Later, a comprehensive study is provided investigating the fracture mechanism in masonry panels tested by Page (1981, 1983). Different loading conditions and different orientations of the panels are considered. Finally, the macroscale approach is outlined, and the results obtained from the mesoscale analysis are employed to identify the material functions appearing in the failure criterion incorporating the scalar anisotropy parameter.

2. Mesoscale formulation and its implementation

The mesoscale analysis of structural masonry requires the information on properties of constituents (bricks, mortar joints) and their geometric arrangement. The constituents themselves may be perceived as isotropic and, in the range of homogeneous deformation, their

mechanical properties can be described by standard continuum approaches. The weakest link in the structural masonry are the brick–mortar interfaces, which require a contact law relating the traction rate to velocity discontinuity. The failure of constituents is often linked with the onset and propagation of localized damage associated with unstable strain-softening response. The onset of localization is usually defined by invoking a stress or energy-based failure criterion or, in case of elastoplastic or damage-based idealization, it may be perceived as a bifurcation problem. The latter involves detection of singularity of the so-called *acoustic tensor* (Rudnicki & Rice, 1975) whose eigenvectors determine the orientation of fracture plane. In this work, the constituents themselves are considered as *elastic*-brittle. Note that there is no conceptual difficulty in considering the bricks/mortar as inelastic. However, in structural masonry the irreversible deformation at the macroscale is primarily due to sliding and separation along the interfaces, so that the former effects seem negligible. In this section, the details on mesoscale modeling are provided. The focus is on the description of deformation process in a domain intercepted by discontinuities, which is relevant for both brick units and interfaces, as the latter are treated as being embedded in the adjacent homogenous continuum.

2.1. Mathematical formulation in the presence of discontinuities

In the presence of localization, the average mechanical properties within a domain containing a fracture may be assessed by incorporating a constitutive law with embedded discontinuity (CLED, cf. Haghighat & Pietruszczak, 2015; Pietruszczak, 1999). For this purpose, consider a referential volume $\Delta\Omega$, which includes the intact parts $\Delta\Omega^+$ and $\Delta\Omega^-$, intercepted by a fractured region of surface area of $\Delta\Gamma_d$ and a negligible thickness (compared to other dimensions). In this case, the discontinuous velocity field $\boldsymbol{v}$ may be defined as a sum of two continuous functions $\widehat{\boldsymbol{v}}$ and $\widetilde{\boldsymbol{v}}$, combined with a discontinuous Heaviside step function $\mathcal{H}_{\Gamma_d}$ as

$$\boldsymbol{v} = \widehat{\boldsymbol{v}} + \mathcal{H}_{\Gamma_d}\widetilde{\boldsymbol{v}}; \quad [\![\boldsymbol{v}]\!] = \boldsymbol{v}^+ - \boldsymbol{v}^- = [\![\mathcal{H}_{\Gamma_d}]\!]\widetilde{\boldsymbol{v}} \tag{1}$$

where $[\![\boldsymbol{v}]\!]$ is the velocity jump across the localized zone. Using Eq. (1), the average velocity gradient in a referential volume $\Delta\Omega$ can be defined as

$$
\begin{aligned}
\nabla_{\mathbf{x}}\boldsymbol{v} &= \frac{1}{\Delta\Omega}\int_{\Delta\Omega}\nabla_{\mathbf{x}}\boldsymbol{v}\ \mathrm{d}\Omega \\
&= \frac{1}{\Delta\Omega}\int_{\Delta\Omega}\nabla_{\mathbf{x}}\widehat{\boldsymbol{v}}\ \mathrm{d}\Omega + \frac{1}{\Delta\Omega}\int_{\Delta\Omega^+}\nabla_{\mathbf{x}}\widetilde{\boldsymbol{v}}\ \mathrm{d}\Omega + \frac{1}{\Delta\Omega}\int_{\Delta\Gamma_d}\left(\widetilde{\boldsymbol{v}}\otimes\nabla_{\mathbf{x}}\mathcal{H}_{\Gamma_d}\right)\mathrm{d}\Omega
\end{aligned} \tag{2}
$$

where

$$\nabla_{\mathbf{x}}\mathcal{H}_{\Gamma_d} = [\![\mathcal{H}_{\Gamma_d}]\!]\delta_{\Gamma_d}\mathbf{n} \tag{3}$$

Here, δ_{Γ_d} is the Dirac delta function and $\mathbf{n}$ is the outward normal to the discontinuity surface. Substituting Eq. (3) into Eq. (2) and using the second equation in (1) leads to

$$
\begin{aligned}
\nabla_{\mathbf{x}}\boldsymbol{v} &= \frac{1}{\Delta\Omega}\int_{\Delta\Omega}\nabla_{\mathbf{x}}\widehat{\boldsymbol{v}}\ \mathrm{d}\Omega + \frac{1}{\Delta\Omega}\int_{\Delta\Omega^+}\nabla_{\mathbf{x}}\widetilde{\boldsymbol{v}}\ \mathrm{d}\Omega \\
&\quad + \frac{1}{\Delta\Omega}\int_{\Delta\Gamma_d}[\![\boldsymbol{v}]\!]\otimes\mathbf{n}\ \mathrm{d}\Gamma_d
\end{aligned} \tag{4}
$$

The first two terms appearing on the right-hand side of Eq. (4) represent the volume average of the velocity gradient in the intact material, while the last term is proportional to the average value of $[\![\boldsymbol{v}]\!]\otimes\mathbf{n}$ over the crack surface area $\Delta\Gamma_d$, i.e

$$\nabla_{\mathbf{x}}\boldsymbol{v}^{(1)} = \frac{1}{\Delta\Omega}\int_{\Delta\Omega}\nabla_{\mathbf{x}}\widehat{\boldsymbol{v}}\ \mathrm{d}\Omega + \frac{1}{\Delta\Omega}\int_{\Delta\Omega^+}\nabla_{\mathbf{x}}\widetilde{\boldsymbol{v}}\ \mathrm{d}\Omega;$$

$$\dot{\mathbf{g}}\otimes\mathbf{n} = \frac{1}{\Delta\Gamma_d}\int_{\Delta\Gamma_d}[\![\boldsymbol{v}]\!]\otimes\mathbf{n}\ \mathrm{d}\Gamma_d \tag{5}$$

The *symmetric* parts of these operators define the corresponding average strain rates. Thus, the total strain rate can be expressed as

$$\dot{\boldsymbol{\varepsilon}} = \dot{\boldsymbol{\varepsilon}}^{(1)} + \chi(\dot{\mathbf{g}}\otimes\mathbf{n})^s \tag{6}$$

where $\dot{\boldsymbol{\varepsilon}}^{(1)} = \left(\nabla_{\mathbf{x}}\mathbf{v}^{(1)}\right)^s$ is the average strain rate in the intact material, while the second term gives the contribution associated with the localized deformation. Here, χ^{-1} is a *length scale parameter* defined as the ratio of the referential volume to the surface area of the fractured region (i.e. $\chi^{-1} = \Delta\Omega/\Delta\Gamma_d$).

The velocity jump $\dot{\mathbf{g}}$ is determined by imposing the traction continuity condition across the localized region. Thus,

$$\dot{\mathbf{t}} - \mathbf{n}\cdot\dot{\boldsymbol{\sigma}} = \mathbf{K}\cdot\dot{\mathbf{g}} - \mathbf{n}\cdot\mathbb{D}\cdot\dot{\boldsymbol{\varepsilon}}^{(1)} = 0 \tag{7}$$

where $\mathbf{t}$ is the traction vector, $\mathbf{K}$ is the second order stiffness operator for the fractured zone, $\dot{\boldsymbol{\sigma}}$ is the macroscopic stress rate and $\mathbb{D}$ is the fourth-order elasticity tensor which defines the properties in the intact region. Combining the above equations and rearranging leads to the localization law

$$\dot{\mathbf{g}} = \left[\left(\mathbf{K} + \chi\mathbf{n}\cdot\mathbb{D}\cdot\mathbf{n}\right)^{-1}\otimes\mathbf{n}\right] : [\mathbb{D} : \dot{\boldsymbol{\varepsilon}}] \tag{8}$$

Finally, using Eqs. (6) and (8), the constitutive relation is obtained as

$$\dot{\boldsymbol{\sigma}} = \overline{\mathbb{D}} : \dot{\boldsymbol{\varepsilon}};$$

$$\overline{\mathbb{D}} = \left\{\mathbb{D} - \chi\mathbb{D} : \left[\mathbf{n}\otimes\left(\mathbf{K} + \chi\mathbf{n}\cdot\mathbb{D}\cdot\mathbf{n}\right)^{-1}\otimes\mathbf{n}\right] : \mathbb{D}\right\} \tag{9}$$

where $\overline{\mathbb{D}}$ is the equivalent tangential stiffness operator which depends on the properties of both constituents and the scale parameter χ, the latter defined at the element level based on the orientation and location of the macrocrack.

2.2. Modeling of constituents

2.2.1. Embedded brick–mortar interfaces

The approach advocated here for FEM analysis is to consider the interfaces as being embedded in the adjacent continuum. Thus, a simple structured mesh may be used, Fig. 1, in which the presence of joints is accounted for by employing standard FEM elements in which mechanical properties are defined by the constitutive law with embedded discontinuity (9). In this case, the discontinuity surface $\Delta\Gamma_d$ is explicitly identified with the brick–mortar interface, which represents the weakest
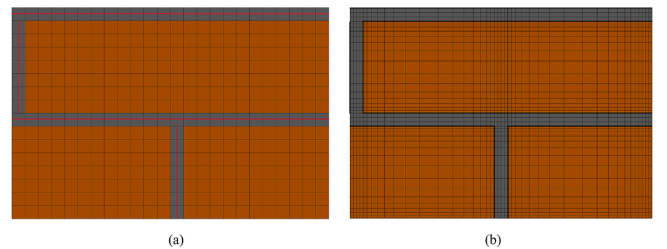

(a)   (b)

Fig. 1. FEM discretization of structural masonry (a) representation incorporating CLED (red line shows interfaces embedded within elements); (b) standard representation incorporating discretization of mortar joints together with interface elements (thick black lines). (For interpretation of the references to colour in this figure legend, the reader is referred to the web version of this article.)

link in the masonry architecture. Fig. 1a show a schematic discretization of a periodic unit with running bond pattern using the proposed methodology. At the same time, Fig. 1b depicts a typical mesh incorporating the physical presence of mortar joints. The latter requires a finer discretization employing a structured mesh together with a set of interface elements. Apparently, the advocated approach is bound to be computationally more efficient. In addition, the numerical problems inherent to the use of interface elements, such as ill-conditioning of the stiffness matrix, poor convergence of the solution and instability of the numerical integration of stress rate equations (cf. Villard, 1996), can be avoided.

The implementation of the proposed methodology requires the specification of the stiffness operator $\mathbf{K}$ appearing in the constitutive relation (9). In the present study, the properties of brick–mortar interface have been described using an elastic-strain softening idealization. In particular, the Coulomb failure function with tension cut-off zone has been employed, i.e.

$$F = \begin{cases} \tau - (c - \mu\sigma) & , \quad \sigma < \sigma_t \\ \sigma - \sigma_t & , \quad \sigma \geq \sigma_t \end{cases} \tag{10}$$

where $\mu = \tan\phi$, with ϕ being the friction angle, and σ, τ represent the magnitudes of normal and tangential components of the traction vector $\mathbf{t}$. Here, $F < 0$ implies an elastic response, while in the plastic regime the degradation functions have been selected as

$$\sigma_t = f_t \exp\left(-\frac{f_t}{G_f} g_n\right); \quad c = c_o \exp(-\alpha g_t) \geq \mu \sigma_t;$$
$$\mu = \mu_o + (\mu_r - \mu_o)\left(\frac{c_o - c}{c_o}\right) \tag{11}$$

Here, the subscripts o and r refer to initial and residual values of c and μ, G_f the is tensile fracture energy release rate, α is a material parameter, while g_n and g_t are normal and shear components of accumulated *plastic* part of displacement jumps.

The equivalent stiffness operator $\overline{\mathbb{D}}$ is determined using Eq. (9), in which $\mathbb{D}$ defines the elastic properties of the adjacent continuum. Here, for $F < 0$ there is $\mathbf{K} = \mathbf{K}^e$, while for an active loading process $\mathbf{K}$ is established using functional forms (10) and (11). In the latter case, a standard plasticity procedure is followed, invoking additivity postulate together with the consistency condition. The framework employed here incorporated an associated flow rule in tension and non-associated (zero-dilatancy) rule in compression regime.

2.2.2. Brick units

The bricks have been also considered here as elastic prior to the onset of localization. The transition was defined via a standard Mohr-Coulomb criterion with Rankin's cut-off, which stipulates that in compression regime the macrocracks form at $\mp(45° + \phi/2)$ with respect to the direction of minor principal stress, whereas in tension their direction is orthogonal to that of maximum tensile stress. The crack propagation process was simulated using the CLED framework, viz. Eq. (9). In the strain-softening regime, the representation analogous to that of eqs. (10)-(11) was employed. However, the degradation law for the friction coefficient was rephrased as

$$\mu = \mu_o + (\mu_r - \mu_o)\left(\frac{c_o - c}{c_o}\right); \quad \mu_o = \frac{\tau - c_o}{\sigma} \tag{12}$$

Thus, in this case the parameter μ_o is not a material constant but is defined explicitly from the condition that, at the onset of localization, the components of traction vector satisfy $F = 0$, Eq. (10). Again, given the functional form (12), the stiffness operator $\mathbf{K}$, Eq. (9), can be determined following the standard plasticity procedure.

As mentioned earlier, for structural masonry the failure mode typically involves fracture along the bed and head joints, whose orientation is defined *a priori*. However, for certain loading histories, the damage process may also involve the onset and propagation of fractures through the brick units. In such a case, a suitable algorithm for a discrete crack tracking is required. In this work, the geometry of propagating crack has been traced by employing the level-set method (Adalsteinsson & Sethian, 1999; Stolarska et al., 2001). The latter is a numerical technique used to represent the location of macrocracks, including the position of their tips. The approach provides information that is particularly useful when dealing with multiple fractures and/or intersecting cracks and allows to quickly locate the potential elements in the vicinity of crack tips, where the fracture is most likely to propagate. The benefits of level-set approach for tracing discrete discontinuities have been discussed extensively in several studies (cf. Stolarska et al., 2001, Belytschko et al., 2001).

According to this approach, a propagating discontinuity surface Γ_d can be defined as the zero level-set of a function $\phi(\mathbf{x}, t)$, i.e., $\Gamma_d = \{\mathbf{x} | \phi(\mathbf{x}, t) = 0\}$. Commonly, the signed distance function expressed as $\phi(\mathbf{x}) = sign\{\mathbf{n} \cdot (\mathbf{x} - \mathbf{x}_\Gamma)\} \min\|\mathbf{x} - \mathbf{x}_\Gamma\|$ is used as a level set function, and it has been employed here for tracing the crack path. The gradient of $\phi(\mathbf{x}, t)$ defines the direction normal to the fracture surface, which is required in implementation of CLED approach. A second level-set is often employed to trace crack tips (Stolarska et al., 2001). Combination of these two level-sets defines a potential zone for fracture propagation and permits tracking of the moving crack without numerical noise.

A schematic example of crack initiation and propagation in a discretized domain is shown in Fig. 2. The initial crack is assumed to pass through the centroid of the element, Fig. 2a, and is shown by the solid red line. The level set function is constructed in the domain, with the zero level-set as depicted by the dashed red line. Elements along the crack path are highlighted in yellow and the crack tip neighbour elements are highlighted in green. An iterative algorithm is then started in which the crack propagates through the crack path elements until equilibrium is reached. Fig. 2b shows the cracked elements (blue) and location of the crack inside the elements. The exact location of the crack in each element is determined using the intercept with the element boundary and the given crack orientation. The level set is updated in the proceeding increment and if stress conditions at the tip elements result in a change in crack direction, the potential elements engaged in further propagation of the cracked zone are identified, as shown in Fig. 2b.

3. Numerical implementation and verification of the mesoscale framework

3.1. Simulation of tests on brick–mortar bond

The first set of numerical examples pertains to simulation of the tensile and shear tests on brick–mortar bond as reported by Van der Pluijm (1997, 2000). The tests were displacement-controlled and
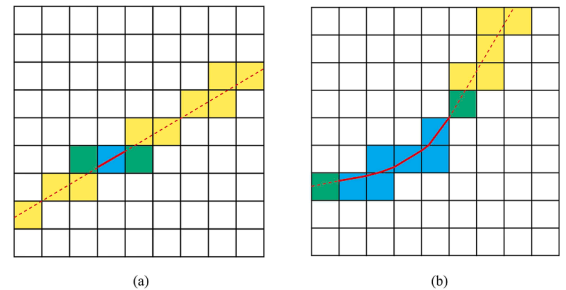

(a)   (b)

Fig. 2. (a) Schematic crack initiation and (b) Crack propagation involving a change in orientation. Dashed line shows the location of zero level set, solid red line and blue elements show crack location, green elements indicate crack tip, yellow elements identify potential elements for crack propagation. (For interpretation of the references to colour in this figure legend, the reader is referred to the web version of this article.)
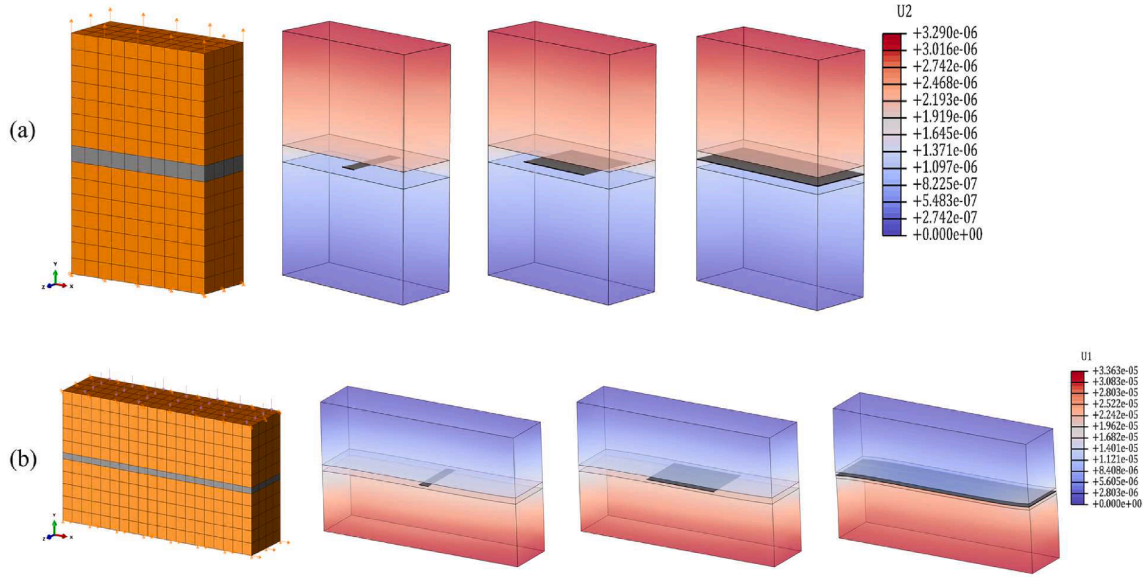
Fig. 3. FEM discretization and evolution of fracture pattern (black) superimposed on (a) vertical displacement field in tension and (b) horizontal displacement field in shear.

were performed on specimens of two brick units, with dimensions $200 \times 100 \times 50$ mm (in shear) and $100 \times 100 \times 50$ mm (in tension), separated by a bed joint. For shear tests, the specimens were subjected to normal stress of intensity between 0.1 and 1.0 MPa, and subsequently sheared by imposing the displacement parallel to the joint. The experimental program was comprehensive, as approx. 50 tests were conducted; however, the scatter of experimental data was significant (i.e., coefficient of variation of 20–40%).

The numerical analysis was conducted using a mesh incorporating 880 and 600 eight-node cubic elements in shear and tension,

respectively. The geometry of the problem and the FEM discretization are shown in Fig. 3. For axial tension, the bottom of the specimen was fixed, and a uniform vertical displacement was applied at the top. For simulations of shear test, the top and the bottom of the sample were fixed in horizontal and vertical directions, respectively. The loading process consisted of applying a vertical force, after which the horizontal displacement was imposed at the bottom surface. The material parameters employed in the analysis are provided in Table 1. The values of these parameters were selected based on the data reported by Van der Pluijm (1993, 1997). Note that the experimental results do not include any explicit information on the material constants that govern the strain softening characteristics, viz. Eq. (11). Therefore, some parametric studies have been conducted on assessing their impact on the numerical predictions.

The main results of simulations are provided in Figs. 3-4. Fig. 3 depicts the evolution of damage along the brick–mortar interface superimposed on the displacement field. The corresponding mechanical characteristics, i.e. traction vs. displacement, are shown in Fig. 4. Here, Fig. 4a depicts the sensitivity of the post-peak response to the selected value of the tensile fracture energy release rate G_f, while Fig. 4b shows the shear characteristics at different values of the normal stress. For the latter case, the results correspond to $\alpha = 10{,}000 \, \text{m}^{-1}$, $\mu_r = 0.85\mu_o$, which gives a fairly close approximation to the experimental data.

Table 1
Material parameters employed in numerical simulations.

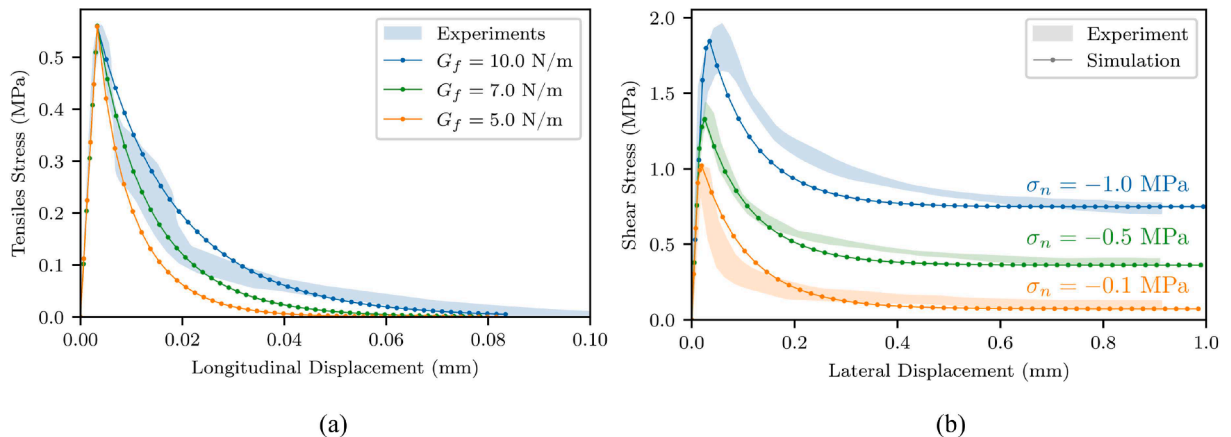|	Brick	Brick-mortar bond
Young's Modulus, E (MPa)	15,000	N/A
Poisson's ratio, v	0.15	N/A
Tensile Strength, f_t (MPa)	3.5	0.65
Angle of internal friction, ϕ (°)	30	36
Cohesion, c (MPa)	19	0.85
Bond normal stiffness, k_n (N/m)	N/A	1.7×10^8
Bond shear stiffness, k_t (N/m)	N/A	7.6×10^8

(a)

(b)

Fig. 4. Mechanical characteristics for the brick–mortar bond in (a) direct tension (influence of fracture energy release, G_f) and (b) shear (influence of normal stress).

Table 2
Material parameters employed in simulations of tensile tests of Backes (1985).

	Brick		Brick-mortar bond	
	Case I	Case II	Case I	Case II
Young's Modulus, E (MPa)	3500	2500	N/A	N/A
Poisson's ratio, v	0.13	0.13	N/A	N/A
Tensile Strength, f_t (MPa)	0.9	1.44	0.12	0.19
Angle of internal friction, ϕ (°)	30	30	30	30
Cohesion, c (MPa)	2.5	1.5	0.25	0.15
Bond normal stiffness, k_n (N/m)	N/A	N/A	0.7×10^8	1.1×10^8
Bond shear stiffness, k_t (N/m)	N/A	N/A	3.2×10^8	3.8×10^8

3.2. Simulation of tensile tests on brick masonry wallets

In order to provide an insight into the fracture propagation mechanism through the masonry constituents, consider first an illustrative example which involves simulation of tensile tests performed by Backes (1985). The tests were conducted on square masonry wallets (490 × 490 × 113 mm) subjected to tension along the direction of bed joints. The analysis here is focused on simulation of two cases which involve two different sets of mechanical properties of constituents as shown in Table 2. Fig. 5a presents the 3D view and the FEM discretization of the wallets, while Figs. 5b-c show the evolution of fracture pattern. For both sets of properties, the tensile cracks initiate in the head

joints. However, the further propagation pattern is affected by the relative values of the shear strength of bed joints and the tensile strength of bricks. A weaker shear strength of brick–mortar bond (e.g. 0.1 – 0.2 MPa) results in a zigzag pattern, while stronger shear bond strength (e.g. 0.2 – 0.9 MPa) leads to formation of tensile cracks inside the bricks. In the latter case, the fracture mode involves formation of a nearly vertical crack penetrating through the head joints and bricks.

Fig. 6 shows the corresponding average stress–strain characteristics. The results correspond to the fracture energy release rates (G_f) of 50 N/m and 10 N/m for the bricks and interface, respectively, while $\alpha = 15,000$ m^{-1} for the bed joints. The predicted structural response at the macroscale is very consistent with the experimental data in terms of both the strength and the deformation response.

3.3. Simulation of biaxial tension–compression tests on structural masonry panels

In order to provide a comprehensive verification of the proposed methodology with respect to combined biaxial tension and compression loading, a set of experimental tests conducted by Dhanasekar et al. (1985) and Page (1983) has been simulated. The focus was on the prediction of fracture pattern and the ultimate load in a broad range of testing configurations. The experiments were conducted on square 0.36 m solid brick masonry panels constructed using half-scale units with dimensions of 115 × 35 × 50 mm. To achieve a uniform stress
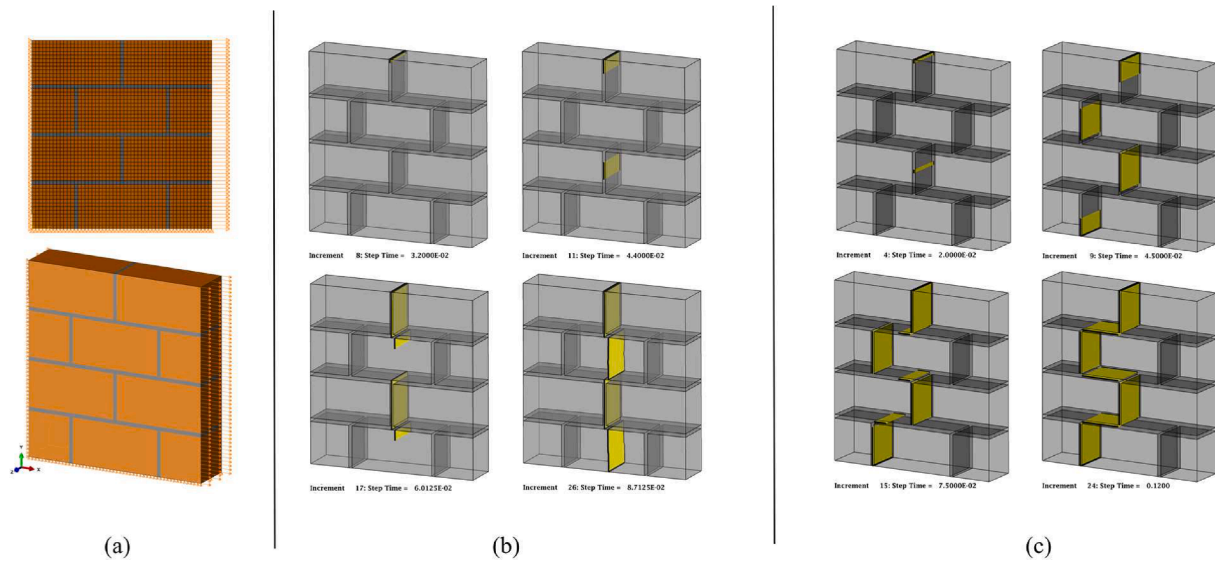

Fig. 5. Uniaxial tension parallel to bed joints: (a) FEM mesh and 3D view; (b) Crack propagation for Case I; (c) Crack pattern for Case II.
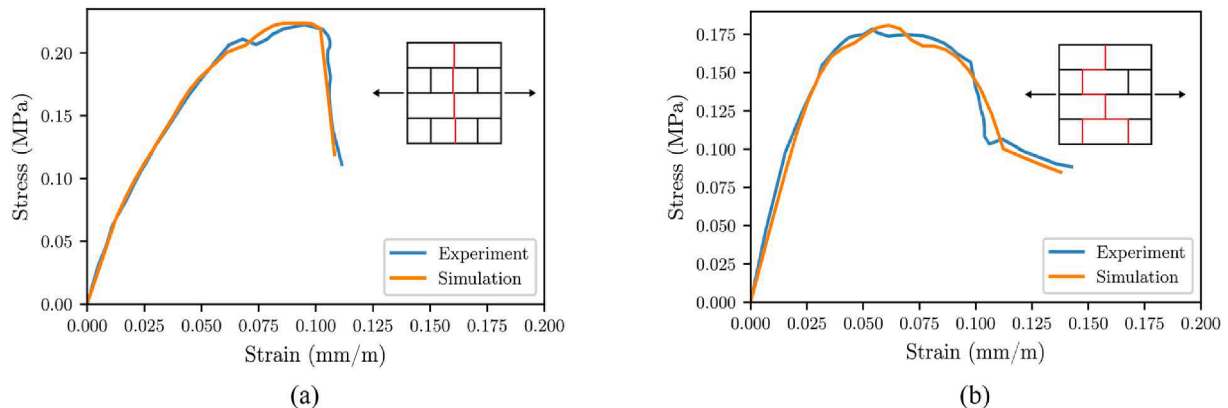

Fig. 6. Average stress–strain characteristics for (a) Case I; (b) Case II (experimental results after Backes (1985); recorded crack patterns are shown schematically).
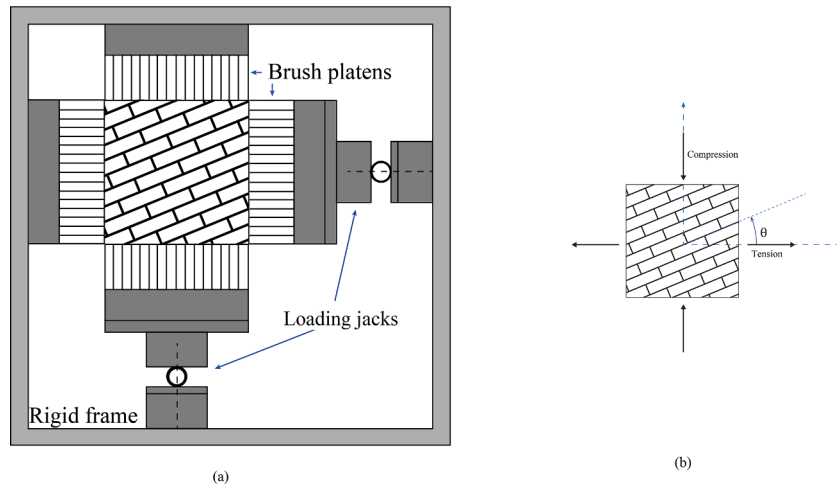
Fig. 7. Experimental setup of Page (1983) and different testing configurations.

distribution along the boundaries and to enable the application of tensile loading, a large number of closely stacked slender elements forming brush-like platens were glued individually to the boundaries of the panel, as illustrated in Fig. 7a. The loading program incorporated uniaxial as well as biaxial tension/compression at different orientations of the bed joints, as shown schematically in Fig. 7b. In all tests, the principal stress directions were fixed while the orientation of the masonry panel was varied. For the majority of tests, the fracture mode involved failure along the masonry joints; however, in some experiments incorporating biaxial loading conditions the onset and propagation of macrocracks within the brick units was also observed.

The geometry of the problem, the boundary conditions and the FEM mesh are shown in Fig. 8. A simple structured mesh, with a total of 15,120 eight-noded cubic elements, was employed in which the presence of brick–mortar bonds has again been accounted for using the CLED formulation. For simulation of uniaxial tests along and normal to bed joints, a displacement-controlled scheme was employed (Fig. 8a); while for other tests, the load-controlled procedure was implemented. The tests on inclined specimens were simulated by transforming the boundary tractions to the principal material axes and applying them as a uniformly distributed load along the respective boundaries, Fig. 8b.

The main challenge in validation of the present approach is a significant variability in the experimental assessment of ultimate load. This stems primarily from a high variation of brick–mortar bond strength as reported in Dhanasekar et al. (1985) and Page (1983). The latter varied between 0.07 and 0.28 MPa with an average of 0.13 MPa. As a result, the bearing capacity of the panel under uniaxial tension perpendicular to bed joints also varied significantly, i.e. between 0.18 and 0.32 MPa with a mean value of 0.24 MPa. An additional issue is incomplete information on properties of constituents. For example, in terms of strength properties of brick units, the only information provided was that on the range of values of compressive strength. Also, no data has been provided on the deformation characteristics of the brick–mortar bond. Given these limitations, some additional parametric studies have been conducted throughout this work. The actual set of material parameters employed in the analysis is provided in Table 3. Here, the properties that were varied through parametric studies (i.e. tensile/shear strength of brick–mortar bond and tensile strength of brick) are displayed in boldface.

Table 3
Material parameters employed in numerical simulations.

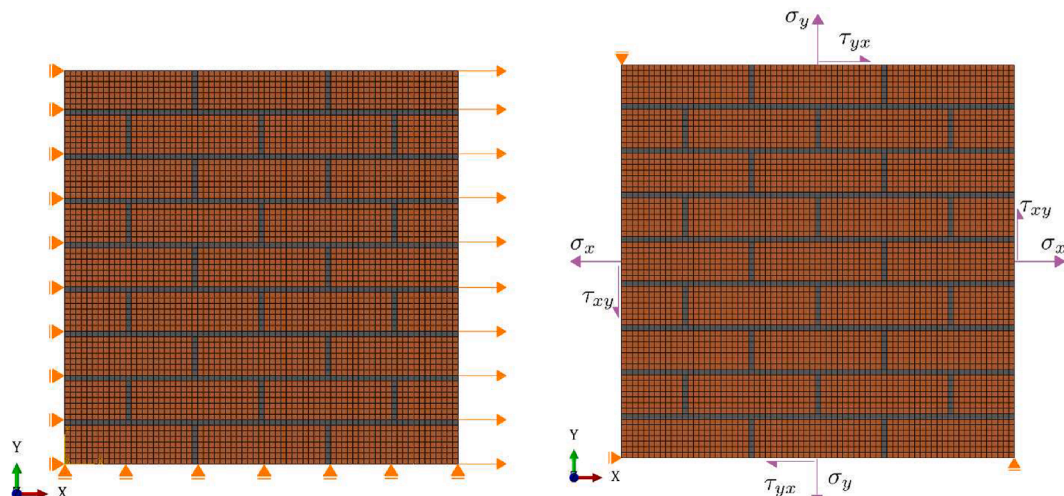| Properties	Brick	Brick-mortar bond
Young's Modulus, E (MPa)	6750	N/A
Poisson's ratio, v	0.17	N/A
Tensile Strength, f_t (MPa)	**1.5**	**0.2**
Angle of internal friction, ϕ (°)	30	39
Cohesion, c (MPa)	4.35	**0.3**
Interface normal stiffness, k_n (N/m)	N/A	1.3×10^8
Interface shear stiffness, k_t (N/m)	N/A	6.2×10^8

Fig. 8. FEM discretization of the panel and the boundary conditions: (a) uniaxial tension; (b) inclined specimens (tractions applied uniformly along the boundaries).
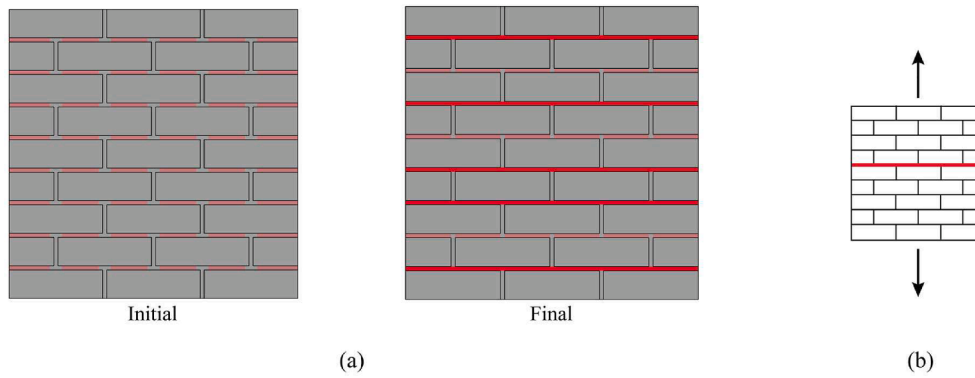
Fig. 9. (a) Evolution of crack pattern and the resulting failure mechanism (bright red colour) for uniaxial tension perpendicular to bed joints ($\theta = 90°$); (b) schematic crack pattern from Page (1983). (For interpretation of the references to colour in this figure legend, the reader is referred to the web version of this article.)

3.3.1. Uniaxial tension tests

The dominant fracture mode in uniaxial tension involves cracking along the brick–mortar interfaces. Depending on the direction of loading with respect to the orientation of bed joints, the tensile fracture in one family of joints may be followed by shear fracture in the perpendicular set of joints. Fig. 9 shows the evolution of damage in case of tension normal to the bedding planes, which are the weakest link within the domain. In this case, the only mode of fracture is a progressive damage along the bed joints, which triggers the failure at the macroscale. The strength of the panel is virtually the same as the tensile strength of the brick–mortar bond. This is shown in Fig. 10 that provides the average
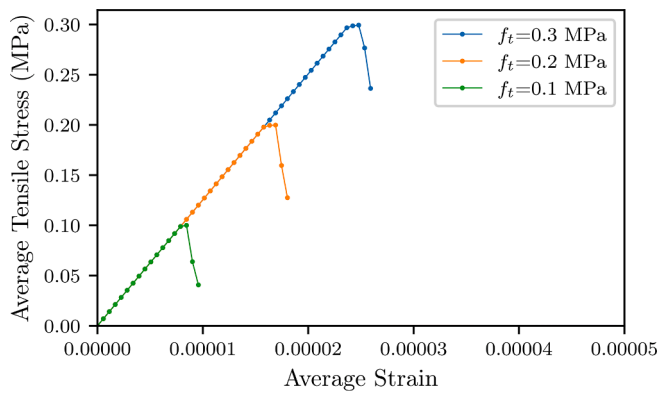
Fig. 10. Average stress–strain characteristics for different tensile strength of brick–mortar bond.

macroscopic stress–strain characteristics for the range of values recorded in the experiment, i.e. 0.1–0.3 MPa.

When the direction of uniaxial tension is parallel to the bedding planes, the tensile fractures start developing within the head joints. For the current set of material parameters, the fracture pattern also involves development of shear fractures in the adjacent bed joints. The combined mechanism of sliding along the bed joints and separation along the head joints causes the global failure at the macroscale. Fig. 11 depicts the evolution of the fracture pattern during the deformation process, while Fig. 12 shows the average stress–strain characteristics. It is evident that, in this case, the ultimate load is quite sensitive to the value of the tensile fracture energy G_f. At the same time, the parameter α which governs the degradation of cohesion, viz. Eq. (11), has no influence on the predicted ultimate stress and affects only the stiffness in the post-peak range.

It should be mentioned that for all load-controlled simulations, the bearing capacity was assessed by monitoring a stability factor (SF) defined as the ratio of the second rate of internal work normalized with respect to that corresponding to the elastic solution (Pietruszczak & Oulapour, 1999). In general, the stability factor remains within the range $1 \geq SF \geq 0$, and $SF = 0$ implies the singularity in the global stiffness operator, i.e. the loss of stability. Fig. 13 depicts the evolution of SF for the present case, i.e. uniaxial tension parallel to bed joints. The results presented here correspond to $G_f = 1 N/m, \alpha = 6000 m^{-1}$ (cf. Fig. 12) and include the average stress–strain characteristics up to the ultimate load obtained for both load-controlled (LC) and displacement-controlled (DC) analyses.

In the case of uniaxial tension at 45°, the onset of fracture occurs in bed joints. Again, as the load increases further the cracks along the head joints develop leading eventually to a zig-zag pattern at the macroscale. This is depicted in Fig. 14, which show a progressive evolution of the
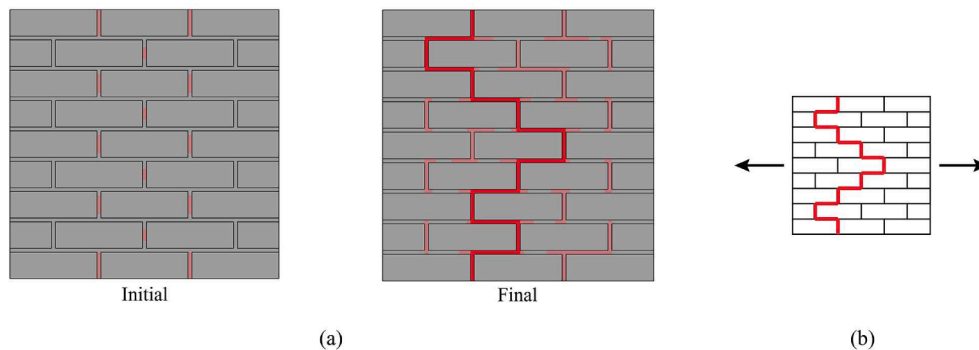

Fig. 11. (a) Evolution of crack pattern and the resulting failure mechanism (bright red colour) for uniaxial tension along the bed joints ($\theta = 0°$); (b) schematic crack pattern from Page (1983). (For interpretation of the references to colour in this figure legend, the reader is referred to the web version of this article.)
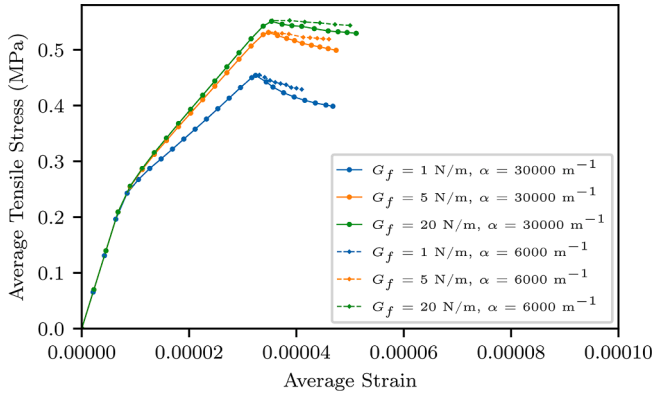
Fig. 12. Average stress–strain characteristics for different values of the tensile fracture energy release G_f and the degradation parameter.α
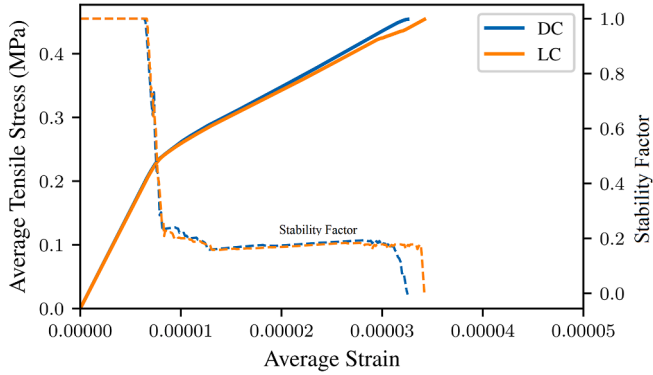

Fig. 13. Evolution of the stability factor (SF) in the panel subjected to uniaxial tension parallel to bed joints.

failure mechanism. The corresponding stress vs. average strain characteristics are presented in Fig. 15. Note that in this case, a load-controlled scheme has been implemented, as described earlier. The ultimate load is significantly affected by the tensile strength of brick–mortar bond, which is evidenced through a parametric study reported in this figure.

3.3.2. Uniaxial compression tests

The primary mode of fracture initiation and propagation in this loading scenario is the tensile splitting of the masonry panel, which occurs not only along the brick–mortar interfaces but also, in some cases, within the brick units. When the direction of loading is parallel to bed joints, the joint interfaces undergo a tensile fracture, forming a set of fracture planes that run through the entire panel. For the compression perpendicular to bed joints, however, the tensile fractures develop in head joints, followed by cracking of the adjacent brick units. This results
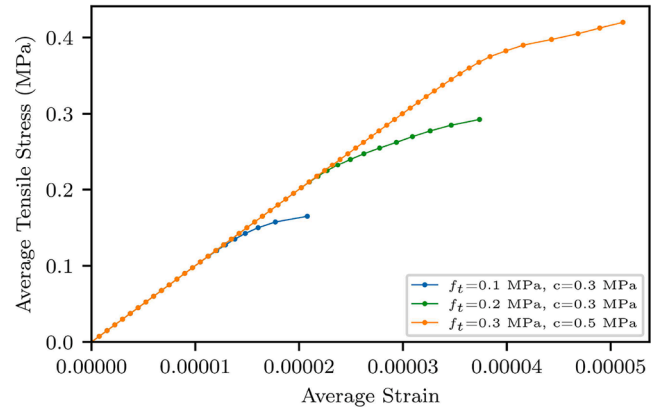

Fig. 15. Average stress–strain characteristics for different values of tensile strength at the brick–mortar interface.

in a higher compressive strength of the panel as compared to other loading directions, as in this case the tensile strength of bricks needs to be attained to trigger a loss of stability.

An important issue to consider in these fracture scenarios is that the failure mechanism does not involve a complete disintegration of the panel at the macroscale. In fact, after formation of tensile splitting planes, the separated parts of the panel act like independent load bearing columns, allowing the panel to sustain significantly higher compressive loads. This part of the mechanical response is not considered in assessing the ultimate bearing capacity in compression, and the formation of a continuous fracture that runs through the panel is perceived as failure. The latter effect is also described in Page (1983) and was used there as the definition of failure at the macroscale. It is noted that this scenario is unlikely to happen in large scale masonry structures, but it is useful for gaining insight into evaluation of the impact of tensile strength of bricks on the ultimate load bearing capacity of masonry panel.

The evolution of fracture mode in uniaxial compression parallel and perpendicular to bed joints is shown in Figs. 16-17. As mentioned earlier, for compression parallel to bed joints, tensile cracks develop in bed joints without triggering the fracture in the bricks. On the other hand, compressive load perpendicular to bed joints causes tensile cracking in head joints followed by initiation of cracks in bricks at the vicinity of the head joints.

3.3.3. Biaxial tension- compression tests

The biaxial tension–compression in two perpendicular directions results in a failure mode that is a combination of those discussed previously. The specific mechanism depends on the actual stress ratio. The testing program reported in Dhanasekar et al. (1985) involved the ratios of
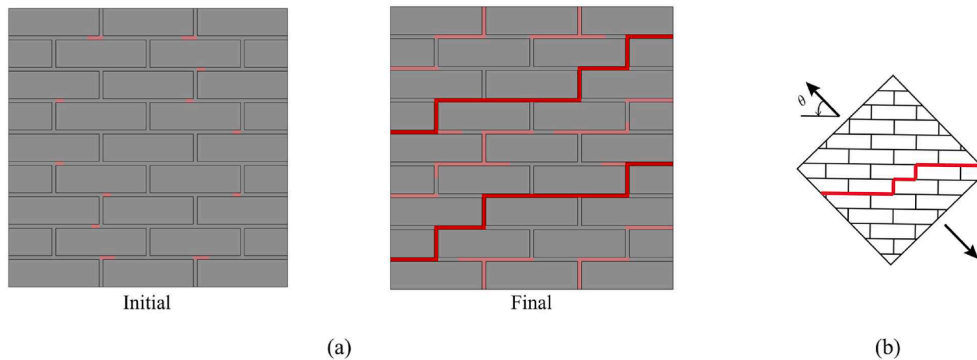

Fig. 14. (a) Evolution of crack pattern and the resulting failure mechanism (bright red colour) for uniaxial tension on inclined panel ($\theta = 45°$); (b) schematic crack pattern from Page (1983). (For interpretation of the references to colour in this figure legend, the reader is referred to the web version of this article.)
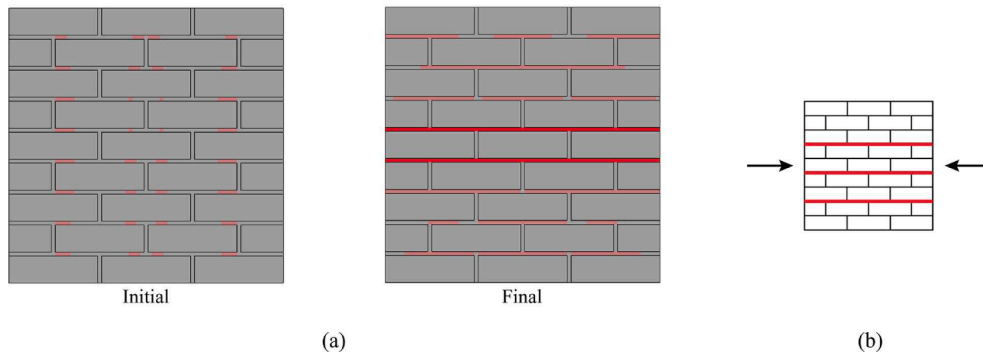
Fig. 16. (a) Evolution of crack pattern and the resulting failure mechanism (bright red colour) (a) for uniaxial compression along the bed joints; (b) schematic crack pattern from Page (1983). (For interpretation of the references to colour in this figure legend, the reader is referred to the web version of this article.)

compressive to tensile load of 2, 5, 10 and 30, and similar values (i.e. 2, 10 and 30) were employed in the current numerical study. The main results of the numerical analysis are provided in Fig. 18, which shows the failure envelopes in the affined space of the major and minor principal stresses. The simulations presented here were carried out for two different values of tensile strength of brick (F_t), i.e. $F_t = 1.0$ and 1.5 MPa, while preserving a constant ratio of 7.5 and 5 between F_t and the

tensile and shear strength of brick–mortar bond (f_t), respectively. Thus, for $F_t = 1.0$ MPa for example, there is $f_t = 0.13$ MPa and $c = 0.2$ MPa.

The first plot in Fig. 18 shows the case of compression perpendicular to bed joints and tension parallel to them (i.e., $\theta = 0°$). In this case, the presence of compressive traction increases the shear resistance in bed joints. As a result, after the onset of cracking along the head joints, the tensile cracks in bricks develop, leading to a higher tensile strength
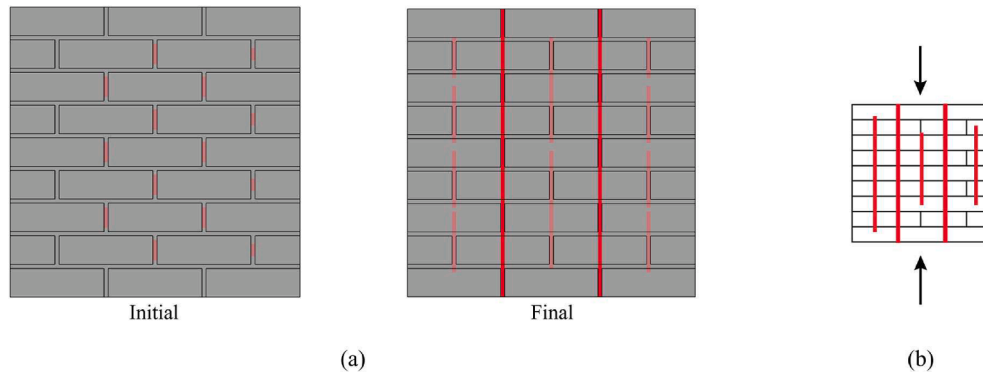

Fig. 17. (a) Evolution of crack pattern and the resulting failure mechanism (bright red colour) (a) for uniaxial compression perpendicular to the bed joints; (b) schematic crack pattern from Page (1983). (For interpretation of the references to colour in this figure legend, the reader is referred to the web version of this article.)
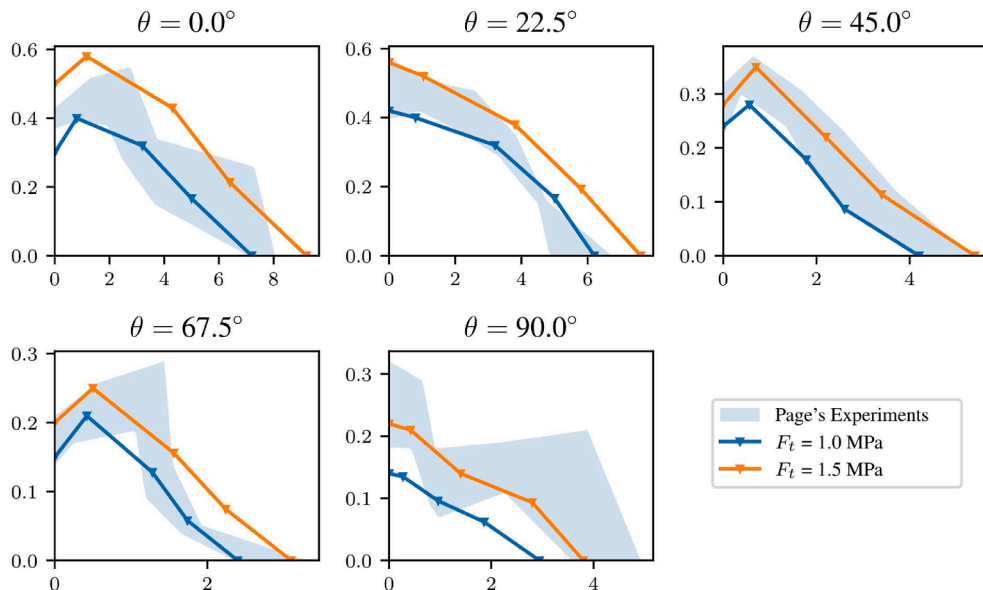

Fig. 18. Failure envelopes for different orientations of the panel (θ) and different tensile strength of masonry units (F_t).

as compared to uniaxial case. As an example, at the stress ratio of 2 and $F_t = 1.5$ MPa, the ultimate tensile and compressive stress values of 0.6 MPa and 1.6 MPa are attained, while the ultimate uniaxial tensile strength is approximately 0.5 MPa.

In the case of compression parallel to bed joints and tension perpendicular to them (i.e., $\theta = 90°$), the response is influenced solely by the bed joints which form a set of continuous weakness planes within the panel. In this situation, an approximately linear transition from ultimate uniaxial compressive strength to ultimate uniaxial tensile strength occurs as the load ratio decreases. The response for other panel orientations, i.e. $\theta = 22.5°$, $45°$, and $67.5°$, has also been simulated and a complete set of results is presented in Fig. 18.

4. Macroscale formulation

The mesoscale approach, as described in Sections 2 and 3, has two primary range of applications; it can be employed for analysis of small-scale masonry structures (e.g. brick walls/arches) and, what is of primary interest here, it can provide a set of 'virtual data' that is required to develop and verify a macroscale approach.

In a macroscale framework, the masonry can be treated as a continuum with a microstructure. In this case, the anisotropic strength/deformation characteristics may be described by adopting a general framework of microstructure tensor approach as outlined in Pietruszczak & Mroz (2001). The approach employs the notion of a scalar anisotropy parameter whose value is a function of relative orientation of the principal stress triad with respect to the preferred directions of microstructure. The macroscopic failure criterion is formulated here by preserving the functional form consistent with mesoscale representation and postulating that the respective strength parameters depend on the orientation of the sample relative to the loading direction. Thus, the mathematical representation incorporates Mohr-Coulomb criterion with Rankine's cut-off in tensile regime, both expressed in terms of stress invariants and enhanced by the notion of directional dependence of strength. The identification of such framework requires the specification of two material functions that describe the variation of friction coefficient and tensile strength with the orientation of the sample relative to the loading direction. Here, an explicit procedure is employed for determination of coefficients of approximation of these functions based on the results of standard axial tension and axial compression tests performed at different orientations of bed joints. For a specific type of masonry, the 'virtual' results of such tests can be generated from the mesoscale simulations, as discussed in Section 3.

Assume that the conditions at failure at the macroscale are governed by the strength criterion expressed in a general form as

$$F = F(I_1, J_2, J_3, \vartheta) = 0 \tag{13}$$

Here, I_1, J_2, J_3, are the basic invariants of stress tensor/deviator, while ϑ is a scalar anisotropy parameter. The latter describes the effect of orientation of principal stress axes in relation to preferred material directions and is defined (after Pietruszczak & Mroz, 2001) as

$$\vartheta = \vartheta_0 \left(1 + \xi + b_1\xi^2 + b_2\xi^3 + b_3\xi^4 + \cdots\right); \tag{14}$$

$$\xi = \ell \cdot \mathbf{A} \cdot \ell$$

In the above expression, ℓ is a unit vector, referred to as a 'loading direction', whose components are the normalized magnitudes of stress vectors acting on planes normal to the material axes. For the structural masonry, the orientation of preferred material axes is defined *a priori* and is identified here with the eigenvectors of the operator $\mathbf{A}$, which is a traceless second-order tensor. Furthermore, the approximation coefficients $\vartheta_0, b_1, b_2, b_3, \cdots$ are constants.

As mentioned earlier, the form of F which is employed in this work, is the Mohr-Coulomb representation with Rankine's cut-off in tensile regime, both incorporating the orientation-dependency of the strength

parameters. Thus

$$F = max(F_1, F_2) = 0;$$

$$F_1 = \sqrt{3}\overline{\sigma} - \eta_f g_1(\Theta)(\sigma_m + C) = 0; \tag{15a}$$

$$F_2 = g_2(\Theta)\overline{\sigma} - (\sigma_m + \sigma_t) = 0$$

where $\overline{\sigma} = (J_2)^{1/2}$, $\sigma_m = I_1/3$, $\Theta = \frac{1}{3}\sin^{-1}\left(\frac{-3\sqrt{3}}{2}\frac{J_3}{\overline{\sigma}^3}\right)$ and

$$g_1(\Theta) = \frac{3 - \sin\phi}{2\sqrt{3}\cos\Theta - 2\sin\Theta\,\sin\phi} \; ; \quad \eta_f = \frac{6\sin\phi}{3 - \sin\phi} \; ;$$

$$g_2(\Theta) = \frac{2}{\sqrt{3}}\sin\left(\Theta + \frac{2\pi}{3}\right); \quad C = c\cot\phi. \tag{15b}$$

Here, Θ is the Lode's angle, while ϕ and c represent the angle of friction and cohesion, respectively. For an isotropic medium η_f and σ_t are material constants, while in case of anisotropy both are variables and are defined in the polynomial form (14), i.e.

$$\eta_f = \widehat{\eta}_f\left(1 + \xi + b_1\xi^2 + b_2\xi^3 + b_3\xi^4 + \cdots\right);$$

$$\sigma_t = \widehat{\sigma}_t\left(1 + \xi + c_1\xi^2 + c_2\xi^3 + c_3\xi^4 + \cdots\right) \tag{16}$$

where b's and c's are the approximation coefficients.

For the purpose of identification of material functions (16), it is convenient to express the representation (15) in terms of principal stress values. Thus

$$F_1 = \frac{1}{2}(\sigma_1 - \sigma_2) + \frac{1}{2}(\sigma_1 + \sigma_2)\sin\phi(\xi) - C\sin\phi(\xi) = 0;$$

$$F_2 = \sigma_1 - \sigma_t(\xi) = 0; \; \sigma_1 > \sigma_3 > \sigma_2 \tag{17}$$

where the tensile stresses are considered as positive.

The preliminary step in the identification procedure is the assessment of the value of parameter C appearing in the Mohr-Coulomb failure condition (15). Note that this parameter is associated with *hydrostatic* tension, and as such it is orientation independent. Furthermore, C has no direct physical significance as the strength in tension regime is governed by the cut-off criterion $F_2 = 0$ in which $max\{\sigma_t\} < C$. Thus, an assessment of C is required only to enable the specification of the material function $\eta_f(\xi)$. Fig. 19 shows the linear best-fit approximations to the numerical data plotted in the affined space $\frac{1}{2}(\sigma_1 - \sigma_2)$ vs. $\frac{1}{2}(\sigma_1 + \sigma_2)$. An estimate of C was obtained by taking the maximum value over the set of configurations considered, which resulted in $C = 0.95$ MPa.

Given the value of C, the next step is to identify the distribution of strength parameter $\eta_f(\xi)$. Referring the problem to the coordinate system in Fig. 7b, with x-axis along the horizontal, the components of loading vector l and unit loading vector ℓ, for a plane stress configuration, become

$$l_1^2 = \cos^2\theta\sigma_x^2 + \sin^2\theta\sigma_y^2;$$

$$l_2^2 = \cos^2\theta\sigma_y^2 + \sin^2\theta\sigma_x^2; \; l_3^2 = 0;$$

$$\ell_1^2 = \frac{l_1^2}{l_1^2 + l_2^2} = \frac{\cos^2\theta\sigma_x^2 + \sin^2\theta\sigma_y^2}{\sigma_x^2 + \sigma_y^2};$$

$$\ell_2^2 = \frac{l_2^2}{l_1^2 + l_2^2} = \frac{\cos^2\theta\sigma_y^2 + \sin^2\theta\sigma_x^2}{\sigma_x^2 + \sigma_y^2}. \tag{18}$$

Assume, as a first approximation, that the material may be perceived as transversely isotropic. In this case, $A_1 = A_3$, which in view of the fact that $\mathbf{A}$ is a traceless operator, implies $A_2 = -2A_1$. Thus, the dyadic product $\xi = \ell \cdot \mathbf{A} \cdot \ell$ may be defined in an explicit form
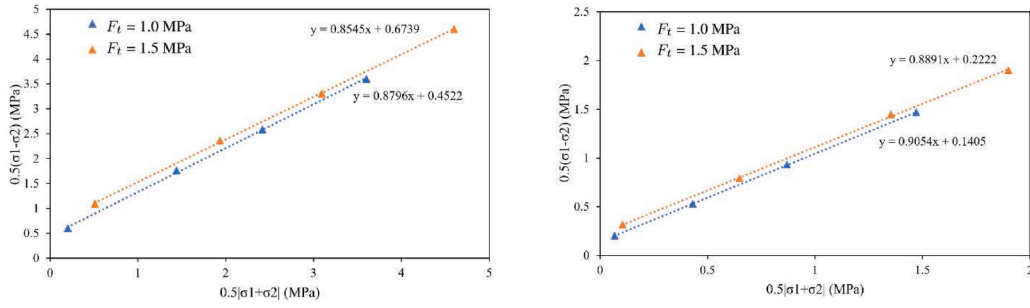
Fig.19. Failure envelopes in compression regime for $\theta = 90°$ and $\theta = 0°$, respectively.

$$\xi = \ell \cdot \mathbf{A} \cdot \ell = A_1 \left(l_1^2 - 2l_2^2 \right)$$

$$= A_1 \left[\frac{\sigma_x^2 \left(1 - 3\sin^2\theta \right) + \sigma_y^2 \left(1 - 3\cos^2\theta \right)}{\sigma_x^2 + \sigma_y^2} \right] \tag{19}$$

in which A_1 is the only independent eigenvalue of $\mathbf{A}$. It is evident that for the uniaxial load, the above expression simplifies to $\xi = A_1 \left(1 - 3\sin^2\theta \right)$.

Fig. 20a shows the best-fit approximation for the function $\eta_f(\xi)$. The results are based on the numerical data for uniaxial compression at different orientations of bed joints. Note that in this case

$$\left. \begin{array}{l} \sigma_1 = f_c \\ \sigma_2 = 0 \end{array} \right\} \rightarrow \sin\phi = \frac{f_c}{f_c + 2C};$$

$$\eta_f = \frac{6\sin\phi}{3 - \sin\phi} = \frac{3f_c}{f_c + 3C} \tag{20}$$

where $f_c = f_c(\xi)$ is the uniaxial compressive strength. The approximations are provided again for two different values of the tensile strength of brick units, viz. $F_t = 1.0$ and 1.5 MPa, which is similar to the parametric study in Section 3.1.3. The mathematical representation incorporates the terms up to the order of three in Eq. (16) and the respective values of coefficients of approximation are given in Table 3.

Fig. 20b shows the best-fit approximation for the function $\sigma_t(\xi)$, which describes the spatial variation of uniaxial tensile strength of the brickwork. Here, the approximations employ again the third-order terms in the dyadic product $\ell \cdot \mathbf{A} \cdot \ell$. The resulting approximation coefficients, for both sets of parameters associated with $F_t = 1.0$ and 1.5 MPa, are given in Table 4.

Finally, Fig. 21 shows the numerical predictions of strength in biaxial tension–compression based on the failure criterion (15). Here, the values of best-fit approximation coefficients provided in Table 4 were employed and the results correspond to $\theta = 0°$, $22.5°$, and $90°$.
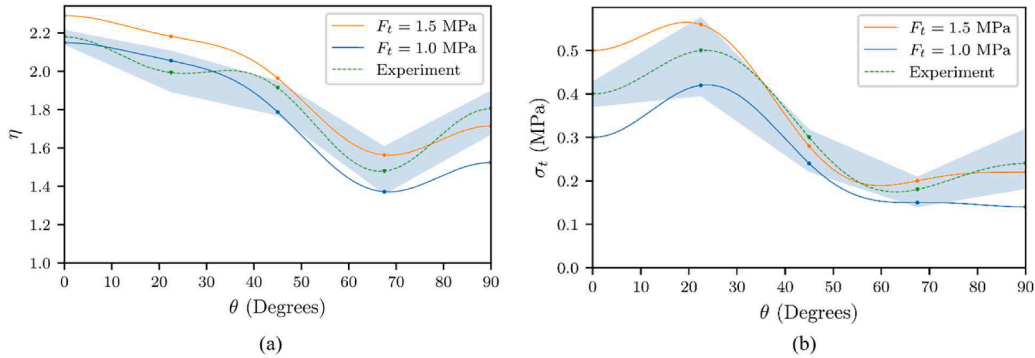

Fig. 20. Best-fit approximations to spatial distribution of strength parameters η_f and σ_t.

Table 4
The coefficients of best-fit approximation for material functions $\eta_f(\xi)$ and $\sigma_t(\xi)$.

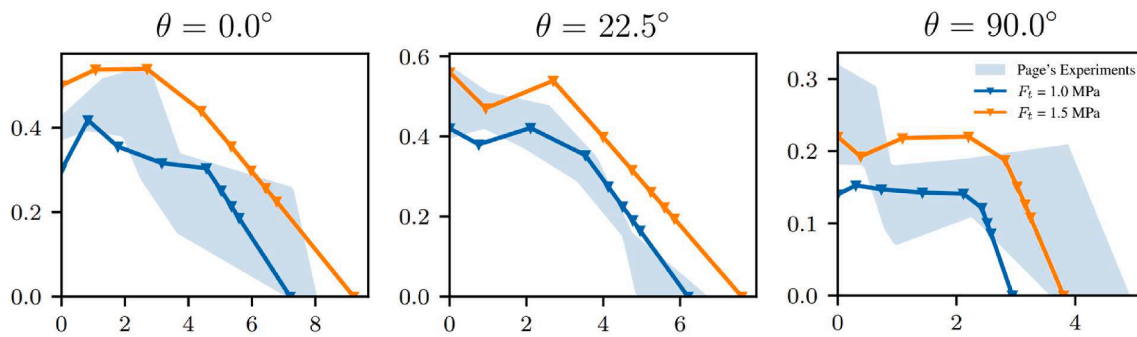|	$\widehat{\eta}_f$	A_1	b_1	b_2	b_3	$\widehat{\sigma}_t$	A_1	c_1	c_2	c_3
$F_t = 1.5 MPa$	2.11	0.089	−10.67	56.56	639.10	0.20	−0.387	5.83	2.34	−10.67
$F_t = 1.0 MPa$	1.96	0.125	−6.09	14.04	159.76	0.17	−0.507	2.84	0.97	−3.93

Fig. 21. Estimated macroscale ultimate strength envelopes for different orientations of the panel (θ) and different tensile strength of masonry units (F_t).

5. Final remarks

The main focus in this work was the development of a computational framework for meso and macroscale analysis of structural masonry. The *mesoscale* approach incorporated a constitutive law with embedded discontinuity to deal with the localized deformation in bed/head joints as well as with the onset and propagation of damage in brick units. In this case, a simple structured FEM has been used in which the brick–mortar interface, which represents the weakest link in the masonry panel, is perceived as being embedded in the adjacent intact medium. For bricks, the level-set method has been employed for tracing the location and propagation of cracks. The proposed methodology yields the results that are not affected by the finite element discretization, which is due to the presence of a length-scale parameter. In addition, the treatment of head/bed joints, as being embedded within a structured mesh, significantly improves the computational efficiency as compared to standard approach that explicitly incorporates all constituents and their interfaces.

The objectives of developing the mesoscale approach are two-fold. On one hand, the framework is suitable for the analysis of small-scale masonry structures. At the same time, it provides a bridging between the two scales, i.e. it serves the purpose of generating 'virtual data' that can be employed for identification of material functions appearing in the macroscale approach. Both these aspects have been illustrated by a number of numerical examples that included the simulations of the tensile and shear tests on brick–mortar bond as reported in Van der Pluijm (1997, 2000) as well as a comprehensive analysis of a set of experimental tests conducted by Dhanasekar et al. (1985) and Page (1983). The latter involved masonry panels subjected to biaxial loading at different orientations of bed joints. For all cases considered, the results have been compared with experimental data, thereby providing a proof-of-concept.

For the *macroscale* approach, only some preliminary work has been reported here. In particular, a procedure for identification of material functions embedded in this framework has been outlined. The latter employed the results of axial compression and tension generated through the mesoscale analysis of panels at different orientation of bed joints. Obviously, a more accurate approximation of these functions may be obtained by also considering the biaxial tension–compression loading.

For the macroscale simulations, an important issue is the specification of the conditions for the onset of localization. In this case, the representation (15) may be phrased in the context of elastoplasticity, so that the localization is perceived as a bifurcation problem. Alternatively, if the conditions at failure are defined through Coulomb and/or Rankine type of criterion, the critical plane approach (Pietruszczak and Mroz, 2001) may be employed whereby the orientation of the localization plane is defined as a constrained optimization problem. Finally, one can also use the 'virtual' data generated from the mesoscale analyses and construct a data-driven neural network that would predict the orientation of macro-fracture for a given stress state. Such an approach could potentially prove to be efficient in engineering applications and will be explored in the follow up studies.

Declaration of Competing Interest

The authors declare that they have no known competing financial interests or personal relationships that could have appeared to influence the work reported in this paper.

Acknowledgement

References

Adalsteinsson, D., Sethian, J.A., 1999. The fast construction of extension velocities in Level Set Methods. J. Comput. Phys. 148 (1), 2–22. https://doi.org/10.1006/jcph.1998.6090.

Alfaiate, J., Simone, A., Sluys, L.J., 2003. Non-homogeneous displacement jumps in strong embedded discontinuities. Int. J. Solids Struct. 40 (21), 5799–5817.

Anthoine, Armelle, 1997. Homogenization of periodic masonry: plane stress, generalized plane strain or 3D modelling? Commun. Numer. Methods Eng. 13 (5), 319–326.

Backes, H.P., 1985. Tensile strength of masonry. In: Proceedings of the 7th International Brick Masonry Conference (Melbourne, Australia). Brick Development Research Institute, pp. 779–790.

Bažant, Z.P., Jirásek, M., 2002. Nonlocal integral formulations of plasticity and damage: survey of progress. J. Eng. Mech. 128 (11), 1119–1149. https://doi.org/10.1061/(ASCE)0733-9399(2002)128:11(1119).

Benkemoun, N., Hautefeuille, M., Colliat, J.-B., Ibrahimbegovic, A., 2010. Failure of heterogeneous materials: 3D meso-scale FE models with embedded discontinuities. Int. J. Numer. Meth. Eng. 82 (13), 1671–1688.

Belytschko, T., Black, T., 1999. Elastic crack growth in finite elements with minimal remeshing. Int. J. Numer. Meth. Eng. 45 (5), 601–620. https://doi.org/10.1002/(ISSN)1097-020710.1002/(SICI)1097-0207(19990620)45:5<>1.0.CO;2-V10.1002/(SICI)1097-0207(19990620)45:5<601::AID-NME598>3.0.CO;2-S.

Belytschko, T., Moës, N., Usui, S., Parimi, C., 2001. Arbitrary discontinuities in finite elements. Int. J. Numer. Meth. Eng. 50 (4), 993–1013. https://doi.org/10.1002/1097-0207(20010210)50:4<993::AID-NME164>3.0.CO;2-M.

Berto, L., Saetta, A., Scotta, R., Vitaliani, R., 2002. An orthotropic damage model for masonry structures. Int. J. Numer. Meth. Eng. 55 (2), 127–157.

Boehler, J.P., Sawczuk, A., 1977. On yielding of oriented solids. Acta Mech. 27 (1), 185–204. https://doi.org/10.1007/BF01180085.

Cluni, F., Gusella, V., 2004. Homogenization of non-periodic masonry structures. Int. J. Solids Struct. 41 (7), 1911–1923. https://doi.org/10.1016/j.ijsolstr.2003.11.011.

Cowin, S.C., 1986. Fabric dependence of an anisotropic strength criterion. Mech. Mater. 5 (3), 251–260. https://doi.org/10.1016/0167-6636(86)90022-0.

De Buhan, P., De Felice, G., 1997. A homogenization approach to the ultimate strength of brick masonry. J. Mech. Phys. Solids 45 (7), 1085–1104. https://doi.org/10.1016/S0022-5096(97)00002-1.

Dhanasekar, M., Kleeman, P.W., Page, A.W., 1985. Biaxial stress-strain relations for brick masonry. J. Struct. Eng. (United States) 111 (5), 1085–1100. https://doi.org/10.1061/(ASCE)0733-9445(1985)111:5(1085).

Drysdale, R.G., Khattab, M.M., 1995. In-plane behavior of grouted concrete masonry under biaxial tension-compression. Structural Journal 92 (6), 653–664.

Feyel, F., 2003. A multilevel finite element method (FE2) to describe the response of highly non-linear structures using generalized continua. Comput. Methods Appl. Mech. Eng. 192 (28-30), 3233–3244.

Geers, M.G.D., Kouznetsova, V.G., Brekelmans, W.A.M., 2010. Multi-scale computational homogenization: Trends and challenges. J. Comput. Appl. Math. 234 (7), 2175–2182. https://doi.org/10.1016/j.cam.2009.08.077.

Haghighat, E., Pietruszczak, S., 2015. On modeling of discrete propagation of localized damage in cohesive-frictional materials. Int. J. Numer. Anal. Meth. Geomech. 39 (16), 1774–1790. https://doi.org/10.1002/nag.v39.1610.1002/nag.2368.

Haghighat, E., Pietruszczak, S., 2016. On modeling of fractured media using an enhanced embedded discontinuity approach. Extreme Mech. Lett. 6, 10–22.

Jirásek, M., 2000. Comparative study on finite elements with embedded discontinuities. Comput. Methods Appl. Mech. Eng. 188 (1-3), 307–330.

Jirásek, M., Zimmermann, T., 2001. Embedded crack model: I. Basic formulation. Int. J. Numer. Meth. Eng. 50 (6), 1269–1290.

Jirásek, M., 2004. Non-local damage mechanics with application to concrete. Revue Française de Génie Civil 8 (5–6), 683–707. https://doi.org/10.1080/12795119.2004.9692625.

Lourénço, P.B., De Borst, R., Rots, J.G., 1997. A plane stress softening plasticity model for orthotropic materials. Int. J. Numer. Meth. Eng. 40 (21), 4033–4057.

Lourénço, P.B., Milani, G., Tralli, A., Zucchini, A., 2007. Analysis of masonry structures: review of and recent trends in homogenization techniques. Can. J. Civ. Eng. 34 (11), 1443–1457. https://doi.org/10.1139/L07-097.

Massart, T.J., Peerlings, R.H.J., Geers, M.G.D., 2007. An enhanced multi-scale approach for masonry wall computations with localization of damage. Int. J. Numer. Meth. Eng. 69 (5), 1022–1059.

Minga, E., Macorini, L., Izzuddin, B.A., 2018. A 3D mesoscale damage-plasticity approach for masonry structures under cyclic loading. Meccanica 53 (7), 1591–1611. https://doi.org/10.1007/s11012-017-0793-z.

Moës, N., Belytschko, T., 2002. Extended finite element method for cohesive crack growth. Eng. Fract. Mech. 69 (7), 813–833. https://doi.org/10.1016/S0013-7944(01)00128-X.

Needleman, A., 1988. Material rate dependence and mesh sensitivity in localization problems. Comput. Methods Appl. Mech. Eng. 67 (1), 69–85. https://doi.org/10.1016/0045-7825(88)90069-2.

Nguyen, V.P., Lloberas-Valls, O., Stroeven, M., Sluys, L.J., 2011. Homogenization-based multiscale crack modelling: From micro-diffusive damage to macro-cracks. Comput. Methods Appl. Mech. Eng. 200 (9-12), 1220–1236.

Niazi, M.S., Wisselink, H.H., Meinders, T., 2012. Viscoplastic regularization of local damage models: A latent solution. Key Eng. Mater. 504–506, 845–850. https://doi.org/10.4028/www.scientific.net/KEM.504-506.845.

Oliver, J., Huespe, A.E., Sánchez, P.J., 2006. A comparative study on finite elements for capturing strong discontinuities: E-FEM vs X-FEM. Comput. Methods Appl. Mech. Eng. 195 (37-40), 4732–4752.

Page, A.W., 1981. The biaxial compressive strength of brick masonry. Proceedings of the Institution of Civil Engineers, ICE Publishing 71 (3), 893–906. https://doi.org/10.1680/iicep.1981.1825.

Page, A.W., 1983. The strength of brick masonry under biaxial tension-compression. Int. J. Masonry Construction 3 (1), 26–31.

Pande, G.N., Liang, J.X., Middleton, J., 1989. Equivalent elastic moduli for brick masonry. Comput. Geotech. 8 (3), 243–265. https://doi.org/10.1016/0266-352X(89)90045-1.

Pietruszczak, S., 1999. On homogeneous and localized deformation in water-infiltrated soils. Int. J. Damage Mech. 8 (3), 233–253.

Pietruszczak, S., Mohammadi, M., 2020. A continuum-based strength criterion for masonry : identification of parameters and validation. Int. J. Masonry Res. Innovation 5 (3), 423–440. https://doi.org/10.1504/IJMRI.2020.108004.

Pietruszczak, S.t., Mróz, Z., 1981. Finite element analysis of deformation of strain-softening materials. Int. J. Numer. Meth. Eng. 17 (3), 327–334.

Pietruszczak, S., Mroz, Z., 2001. On failure criteria for anisotropic cohesive-frictional materials. Int. J. Numer. Anal. Meth. Geomech. 25 (5), 509–524. https://doi.org/10.1002/(ISSN)1096-985310.1002/nag.v25:510.1002/nag.141.

Pietruszczak, S., Oulapour, M., 1999. Assessment of dynamic stability of foundations on saturated sandy soils. J. Geotech. Geoenviron. Eng. 125 (7), 576–582. https://doi.org/10.1061/(asce)1090-0241(1999)125:7(576).

Van der Pluijm, R., 1993. Shear behaviour of bed joints. Proceedings of 6th North American Masonry Conference, Philadelphia, Pennsylvania, USA 125–136.

Van der Pluijm, R., 1997. Non-linear behaviour of masonry under tension. Heron Journal-English Edition 42 (1), 25–54. ISSN 0046-7316.

Van der Pluijm, R., Rutten, H., & Ceelen, M. (2000). Shear behaviour of bed joints. *12th International Brick/Block Masonry Conference (Madrid, Spain), Historical and Masonry Structures, Minho University Publication.*

Rudnicki, J.W., Rice, J.R., 1975. Conditions for the localization of deformation in pressure-sensitive dilatant materials. J. Mech. Phys. Solids 23 (6), 371–394. https://doi.org/10.1016/0022-5096(75)90001-0.

Sacco, E., 2009. A nonlinear homogenization procedure for periodic masonry. European Journal of Mechanics-A/Solids 28 (2), 209–222.

Simo, J.C., Oliver, J., Armero, F., 1993. An analysis of strong discontinuities induced by strain-softening in rate-independent inelastic solids. Comput. Mech. 12 (5), 277–296. https://doi.org/10.1007/BF00372173.

van der Sluis, O., Schreurs, P.J.G., Brekelmans, W.A.M., Meijer, H.E.H., 2000. Overall behaviour of heterogeneous elastoviscoplastic materials: effect of microstructural modelling. Mech. Mater. 32 (8), 449–462.

Smit, R.J.M., Brekelmans, W.A.M., Meijer, H.E.H., 1998. Prediction of the mechanical behavior of nonlinear heterogeneous systems by multi-level finite element modeling. Comput. Methods Appl. Mech. Eng. 155 (1-2), 181–192.

Stolarska, M., Chopp, D.L., Moës, N., Belytschko, T., 2001. Modelling crack growth by level sets in the extended finite element method. Int. J. Numer. Meth. Eng. 51 (8), 943–960. https://doi.org/10.1002/nme.201.

Tsai, S.W., Wu, E.M., 1971. A general theory of strength for anisotropic materials. J. Compos. Mater. 5 (1), 58–80. https://doi.org/10.1177/002199837100500106.

Villard, P., 1996. Modelling of interface problems by the finite element method with considerable displacements. Comput. Geotech. 19 (1), 23–45.

Wells, G.N., Sluys, L.J., 2000. Application of embedded discontinuities for softening solids. Eng. Fract. Mech. 65 (2-3), 263–281.

Wells, G.N., Sluys, L.J., 2001. Three-dimensional embedded discontinuity model for brittle fracture. Int. J. Solids Struct. 38 (5), 897–913.